Journal of Alloys and Compounds 928 (2022) 167028

Contents lists available at ScienceDirect

Journal of Alloys and Compounds

journal homepage: www.elsevier.com/locate/jalcom

Hot deformation behavior and constitutive modeling of a cost-effective $Al_8Cr_{12}Mn_{25}Ni_{20}Fe_{35}$ high-entropy alloy

Ahmed W. Abdelghany[a,b,*], Matias Jaskari[c], Atef S. Hamada[c], Antti Järvenpää[c], Hassan A. El-Hofy[d], Akihiko Chiba[e], Mohamed Abdel-Hady Gepreel[a]

[a] Materials Science and Engineering Department, School of Innovative Design Engineering, Egypt-Japan University of Science and Technology, Alexandria 21934, Egypt
[b] Design and Production Engineering Department, Faculty of Engineering, Ain Shams University, Cairo Governorate 11535, Egypt
[c] FMT-group, Kerttu Saalasti Institute, University of Oulu, Pajatie 5, FI-85500 Nivala, Finland
[d] Industrial and Manufacturing Engineering Department, School of Innovative Design Engineering, Egypt–Japan University of Science and Technology, Alexandria 21934, Egypt
[e] Institute for Materials Research, Tohoku University, 2-1-1 Katahira, Aoba-ku, Sendai 980-8577, Japan

ARTICLE INFO

Article history:
Received 28 June 2022
Received in revised form 12 August 2022
Accepted 28 August 2022
Available online 31 August 2022

Keywords:
High-entropy alloy design
Non-equiatomic
AlCrMnNiFe
Hot deformation behavior
Microstructural evolution
Dynamic recrystallization
Flow stress
Constitutive equation

ABSTRACT

In this study, a new non-equiatomic and cost-effective high-entropy alloy (HEA), $Al_8Cr_{12}Mn_{25}Fe_{35}Ni_{20}$, was designed using thermodynamic parameters and prepared by arc melting. The alloy was subjected to homogenization at 1200 °C and a hot-rolling reduction of 50%. The hot deformation behavior and deformation mechanism were studied at varying strain rates ranging from 0.01 to 10 s^{-1} and temperatures ranging from 900° to 1100°C via plane strain compression tests using a Gleeble 3800 thermo-mechanical simulator. The phase structure of the rolled alloy was studied using electron backscattered diffraction (EBSD), X-ray diffraction, and differential thermal analysis to detect phase transformation. The constitutive model was implemented to predict the high-temperature flow stress using the Zener-Holloman parameter (Z), which correlated well with the experimental values. The studied HEA exhibited a relatively high activation energy for hot deformation of 389.5 $kJ.mol^{-1}$, i.e., comparable to those of equiatomic HEAs in the literature. The hot-deformed microstructural features and deformation mechanism were studied using EBSD, which revealed discontinuous dynamic recrystallization as the main softening mechanism. Dynamic recrystallization (DRX) showed the formation of fine grains along the initial grain boundaries, accompanied by Al-Ni-rich B2 precipitates at the recrystallized grain boundaries.

1. Introduction

High-entropy alloys (HEAs), with multiple elements mixed at equal or near-equal molar ratios, have led to breakthroughs in the field of materials science owing to their superior properties compared with traditional alloys. Therefore, they have attracted significant attention for both research and industrial applications [1]. Contradicting the concept of the conventional alloy system, which is based on one principal element, and enhancing the properties by adding relatively small amounts of other elements, HEAs mix elements with high atomic percentages ranging from 5 to 35 at %, thereby considering all elements as principal. HEAs are attracting increasing interest for advanced functional applications [2] owing to their remarkable mechanical properties, which could for example, overcome the strength-ductility paradox associated with traditional alloys [3,4] and enhance high-temperature properties [5]. This new concept represents a paradigm shift in the revolution of alloy development, and research in this field is extensively increasing worldwide. Therefore, HEAs have become a developing class in the new field of advanced materials. Raabe et al. [6] introduced the concept of high-entropy steels, and according to this concept, some stainless steels and even superalloys can be categorized as HEAs [7].

Abbreviations: HEA, High Entropy Alloy; EBSD, Electron BackScattered Diffraction; DRX, Dynamic Recrystallization; VEC, Valence Electron Concentration; SFE, Stacking Fault Energy; DRV, Dynamic Recovery; GBS, Grain Boundary Sliding; KPI, Key Parameter Indicator; SSS, Simple Solid Solution; SSSI, Solid Solution Selection Index; XRD, X-ray Diffraction; DTA, Differential Thermal Analysis; IPF, Inverse Pole Figure; LAGB, Low Angle Grain Boundaries; HAGB, High Angle Grain Boundaries; DDRX, Discontinuous Dynamic Recrystallization; SIBM, Strain Induced Boundary Migration; KAM, Kernel Average Misorientation

* Correspondence to: Visiting Researcher at FMT-group, Kerttu Saalasti Institute, University of Oulu, Pajatie 5, FI-85500 Nivala, Finland.
E-mail address: ahmed.wagdy@eng.asu.edu.eg (A.W. Abdelghany).

https://doi.org/10.1016/j.jallcom.2022.167028

Alloy design and phase stability are crucial for the development of new alloys. In the past decade, extensive efforts have been made by researchers to formulate a method for designing HEAs. Thermodynamic parameters obtained using empirical formulas are widely used guides for alloy design. Moreover, the commonly used Mo-Bd method in Ti alloys has also been introduced for HEAs employing Ti for biomedical applications [8,9]. Tapia et al. [10] presented a parametric study of single-phase HEAs using an in-house thermodynamic database. Another study surveyed 370 different HEAs and collected the mechanical properties reported in a specific study period [11]. Owing to the extensive data analysis required for proper alloy selection, a machine learning approach has been introduced to HEA design [12]. Moreover, HEAs are argued to have a relatively high-cost because most elements used in the proposed compositions are expensive. Fu et al. [13] presented a quantitative analysis in which the elements used in HEAs over the past decade were categorized according to their price and availability. The analysis classified the elements with a cost of ~$0.5/mol as low-price elements, which were as follows: Al, Cr, Cu, Fe, Le, Mg, Mn, Ni, Pb, Sb, Si, Ti, and V.

To explore the usage of low-cost elements in HEA design, Elkatatny et al. [14] introduced a new cost-effective non-equiatomic $Al_5Cr_{12}Mn_{28}Fe_{35}Ni_{20}$ HEA. In addition, Shaysultanov et al. [15] proposed a dual-phase face-centered cubic (FCC) and BCC/B2 HEA composed of $Al_{10}Cr_{18}Mn_{21}Fe_{36}Ni_{15}$. The Al concentration was reported to have a critical effect on HEA strengthening because of its large atomic size, which directly increases the lattice distortion, as well as acts as a BCC stabilizing element [14,16]. Nevertheless, other researchers concluded that Al would stabilize BCC/B2 only at a certain composition range (i.e., $X_{Al} \leq 0.6$ at%) and would enhance the FCC stabilization at higher percentages correlated to the valence electron concentration (VEC) effect [14,17]. Another study by Ogura et al. [18] determined that adding Al to the equiatomic CrFeCoNi HEA reduced the BCC energy of formation and increased that of FCC. Moreover, according to the local energies, Cr and Fe act as BCC stabilizers in opposition to the FCC stabilizing effect of Ni and Co.

Another promising cost-effective element for HEAs is Mn. Haase et al. [19] compared high manganese steel (HMnS) to other HEAs containing high percentages of Mn. Reuniting the modern strengthening concept to activate strengthening mechanisms at an appropriate time, the high manganese content in HMnS improved plasticity owing to its low stacking fault energy (SFE) [20]. The mechanical properties can be enhanced by activating either martensitic transformations or mechanical twinning to achieve higher strength and larger elongation, facilitating low-temperature industrial applications such as in the automotive sector. As a result, a lower dynamic recovery rate and different deformation mechanisms are expected [21].

Optimization of the mechanical properties of HEAs is critical to their successful in promising application. The poor mechanical properties of HEAs in the as-cast condition (i.e., strength–ductility combination) are related to the existence of coarse columnar structures and elemental segregation [22]. Therefore, homogenization and breaking of the cast structure of the alloy is an important process for optimizing the mechanical properties of HEAs. Generaly, the thermomechanical treatment is an efficient approach that can be applied to cast HEAs. Furthermore, the hot deformation characteristics of HEAs are key for the efficient design of the processing regime (e.g., hot-rolling/forging), along with controlling the grain structure and optimizing the mechanical properties. Kaypour et al. [23] studied the effect of Al addition to equiatomic MnCrCoFeNi on the high-temperature compressive behavior and concluded that the work hardenability of the alloy increased with Al addition. The hot deformation behavior of CoCrFeMnNi reported by Eleti et al. [24] showed that dynamic recrystallization (DRX) was initiated at the initial grain boundaries, and a necklace structure was observed. A study by Tian et al. [25] on the hot deformation of lightweight AlCoCrFeNi determined that the sensitivity of the softening mechanism is more dependent on the deformation temperature. The softening effect was primarily controlled by the dynamic precipitation of the FCC and dynamic recovery (DRV). The flow stress softening mechanism was attributed to grain boundary sliding (GBS) at relatively low temperatures ranging from 800° to 900°C. On the other hand, DRV and DRX were attributed to the softening mechanism at a higher temperature of 1100 °C. In light of the increasing interest in HEAs over the past decade, further research is required to gain a deeper understanding of their behavior under hot deformation.

This study aims to implement the thermodynamic design concepts of HEAs to design a new cost-effective HEA $Al_8Cr_{12}Mn_{25}Fe_{35}Ni_{20}$ with a single FCC structure. Furthermore, we experimentally tested the high-temperature deformation behavior of the HEA under study and the resulting microstructure development at different temperatures and strain rates. The constitutive model and the Zener-Hollomon equation are presented in this paper, which can be generalized for further optimization of the processing conditions of the studied HEA.

Table 1
Quantitative guiding empirical parameters for HEAs (criteria and key parameter indicator (KPI)).

Criteria	KPI rule	Solid solution condition	Ref.
Formation of Simple Solid Solution (SSS)	$\Delta H_{mix} = \sum_{i=1, i\neq j}^{N} 4\,\Delta H_{AB}^{mix} \cdot c_i c_j$	$-22 \leq \Delta H_{mix} \leq 7 \quad (\frac{kJ}{mol})$	[28,29]
	$\Delta S_{mix} = -R\sum_{i=1}^{N} c_i \ln c_i$	$1.32R \leq \Delta S_{mix} \leq 2.34R$ (J. K^{-1}. mol^{-1}), where R is the gas constant	[2]
Single Phase Solid Solution (SPSS)	$\delta\% = 100 \cdot \sqrt{\sum_{i=1}^{N} c_i \left(1 - \frac{r_i}{\bar{r}}\right)^2}$	Atomic size mismatch, δ $\delta \leq 6.6\%$, will enhance the chance of obtaining a SPSS structure where: $\bar{r} = \sum_{i=1}^{N} c_i r_i$	[30]
High-entropy phase(s)	$\Omega = \frac{T_m \Delta S_{mix}}{\lvert \Delta H_{mix} \rvert}$	Generally, when $\Omega > 1.1$ the effect of the mixing entropy is greater than that of the enthalpy of mixing at the melting temperature.	[30]
Melting Temperature	$T_m = \sum_{i=1}^{N} c_i (T_m)_i$	Calculated by the rule of mixtures	[31]
Probable phases tend to form	$VEC = \sum_{i=1}^{N} c_i (VEC)_i$	$VEC \leq 6.87 \rightarrow$ (FCC) $6.87 < VEC < 8.0 \rightarrow$ (BCC + FCC) $VEC \geq 8.0 \rightarrow$ (BCC)	[30,31]
	$SSSI = \sum_{i=1}^{N} c_i \beta_i$	β_i represents the stabilizing ability of element i. +ve = FCC stabilizing -ve = BCC/B2 stabilizing	[27]
Electronegativity difference	$\Delta\chi = \sqrt{\sum_{i=1}^{N} c_i \left(\chi_i - \sum_{j=1}^{n} c_j \chi_j\right)^2}$	χ_i and χ_j are the Pauling electronegativity for the i^{th} and j^{th} element, respectively. The quantitative criterion of electronegativity difference must be $\Delta\chi \leq 1$	[2]

Table 2
Values used in the calculation of thermodynamic parameters: Mixing enthalpy ΔH_{AB} for A-B elements, atomic radius (r), melting temperature (T_m), and stabilizing ability of each element (β_i) [27,32,33].

			ΔH_{AB} (kJ/mol)		
Al	0				
Fe	-11	0			
Ni	-22	-2	0		
Mn	-19	0	-8	0	
Cr	-10	-1	-7	2	0

	Al	Fe	Ni	Mn	Cr
r (Å)	1.4317	1.2412	1.2459	1.3500	1.2491
T_m (°K)	934	1811	1728	1519	2180
β_i	-0.85	-0.41	+ 1	-0.59	-0.37

2. Alloy design and experimental procedures

2.1. HEA design and modeling

The general properties of HEAs can be customized if the tendency for a certain phase formation is predicted, for example, by enhancing the BCC/B2 stability and/or decreasing the FCC stability for dual-phase structures and vice versa for a single FCC or BCC structure. Table 1 summarizes the thermodynamic parameters and the key parameter indicator (KPI) for each rule, including the mixing entropy (ΔS_{mix}), mixing enthalpy (ΔH_{mix}), Gibbs free energy (ΔG_{mix}), valence electron concentration (VEC), atomic size difference (δ), and calculated melting temperature (T_m). The values for the formation of a simple solid solution for each parameter are also listed in Table 1.

Integrating the concept of a simple solid solution (SSS), ΔH_{mix} is one of the KPIs for this criterion derived from the enthalpy of mix for binary alloys. The enthalpy values for every two elements used in this study are listed in Table 2, along with the corresponding atomic radii and melting temperatures for calculating δ and T_m, respectively. The probable phase to be formed can be predicted using the VEC rule. However, an argument to the contrary was made in a recent study by Yang et al. [26], who proposed a new approach known as the effectiveness of the VEC rule (EVEC). However, this approach cannot predict the stability of dual-phase regions such as the FCC + BCC phases. Another new parameter introduced by Kube et al. [27] is the solid solution selection index (SSSI), which can be used to predict the formation of phases in which a high tendency to form an FCC structure is included at an index value of + 1 and BCC/B2 at − 1, while the SSSI ranges between these values. The SSSI is calculated by the rule of mixtures using the newly introduced factor β_i, which represents the stabilizing ability of each element. Table 2 shows the different factors for the five elements used in this study, where (β_{Al}) is the highest BCC/B2 stabilizing element (−0.85), whereas Ni has a greater ability to stabilize the FCC structure where (β_{Ni} = +1).

The suggested composition was determined by calculating and evaluating the relevant thermodynamic parameters of the different composition systems. The effects of Mn and Al content on the thermodynamic values of $Al_xCr_{12}Ni_{20}Mn_zFe_{68-x-z}$ are shown in Fig. 1, where Al at% varies along the x-axis and Mn at% along with different graph line plots. The figures indicate that both Al and Mn at% have the same effect on the parameters shown. However, the effect of Al is generally greater than that of Mn. The horizontal dotted line in Fig. 1(a) represents the value of 1.5 (ΔSmix/R), where the HEAs are defined around and higher than this value. For example, for simple solid solution (SSS) formation, at 20 at% of Mn, it can be inferred that an atomic percentage of Al greater than 10% is required to achieve that value. The graph suggests the use of 25–30 at% of Mn with Al ranging from 7.5 to 8.5 at%. Fig. 1(b) shows the effect of the elements on the enthalpy of mixing, and it is concluded that for SSS, all constituent percentages satisfy the range $-22 \le \Delta H_{mix} \le 7(\frac{kJ}{mol})$. It is worth noting that increasing the Al at% significantly increases the $|\Delta H_{mix}|$ for the entire alloy; thus, the value of parameter Ω decreases. The last parameter (Ω) indicates the relationship between the entropy of mixing at the melting temperature and the mixing enthalpy; thus, a solid solution would form if this value is higher than 1.1. The difference in atomic sizes indicates lattice distortion of the HEA lattice, which directly affects both the mechanical properties and phase stability. It can be concluded that Mn does not significantly affect δ% when compared to Al, which would significantly change this value and dramatically affect the mechanical performance and/or phase stability. This is directly attributed to the large atomic size of Al (Table 2) when compared to other elements. Therefore, a serious concern should be taken for the Al at% value that plays a major role in achieving the desired properties.

The final selected elemental composition for this study was $Al_8Cr_{12}Ni_{20}Mn_{25}Fe_{35}$, designated as Fe-HEA, as Fe is the main element in the alloy. The thermodynamic values of the Fe-HEA are summarized in Table 3, along with a comparison of previously studied promising HEAs with the same elemental compositional range. From the values shown, it can be concluded that the Fe-HEA thermodynamic values lie between those of the previously studied HEAs, where the $Al_5Cr_{12}Mn_{28}Fe_{35}Ni_{20}$ was entirely FCC and the $Al_{10}Cr_{18}Mn_{21}Fe_{36}Ni_{15}$ was a dual FCC/BCC phase structure. The alloy with 10 at% Al showed better mechanical performance than that containing 5 at% Al. From the β_i values, it can be determined that Ni was the highest FCC stabilizing element. Nevertheless, the calculated SSSI value was found to be negative for all HEAs, as shown in Table 3. The SSSI would need to be quantitatively evaluated for further application and precise prediction (e.g., previously studied $Al_5Cr_{12}Mn_{28}Fe_{35}Ni_{20}$ forms a full FCC structure and the SSSI value is −0.2). However, it can be used as an effective qualitative index to determine the direction of the phase stabilization.

The Thermo-Calc software with the TCHEA4 database version 2022a was used to predict the equilibrium phases, volume fraction, and transformation temperature. Fig. 2 shows the isopleth equilibrium phase diagram of Fe-HEA. The Thermo-Calc database results are consistent with the previously suggested design methodology for the high FCC phase formation. It is observed that the metastable BCC/B2 phase is formed at a temperature of 1520 °C, whereas a disordered FCC structure is promoted at the end of solidification at a temperature of 1320 °C, bearing the BCC/B2 phase. Furthermore, its volume fraction increases to a value ˃ 90% at a temperature slightly below 1100 °C.

2.2. Alloy preparation

A HEA with five components, $Al_8Cr_{12}Mn_{25}Fe_{35}Ni_{20}$ (Fe-HEA), was prepared using a single-electrode electric arc furnace (ARCAST 200, USA), equipped with a water-cooled copper crucible. Ingots of 200 g each were melted from high-purity elements (Al, Cr, Mn, Fe, and Ni) in an argon atmosphere, and then flipped and re-melted thrice while applying electromagnetic stirring at the end of each melting cycle to ensure homogenization and heat distribution on the final ingot. The ingots were then left to cool in a Cu crucible. A square specimen of size 30 mm × 30 mm was then analyzed using a PANalytical AXIOS XRF spectrometer to determine the chemical composition of the Fe-HEA after melting. A comparison between the nominal and chemically-analyzed results is presented in Table 4.

A viable approach for the mass production and commercialization of HEAs is casting, followed by secondary processing. Li and Raabe [34] proposed a processing regime for 3D transition metal HEAs. The processing includes homogenization at a temperature of 1200 °C for 2–5 h to obtain a compositionally homogenous structure, followed by hot forming at high temperatures that enhanced the strength and ductility [3]. Table 5 lists the homogenization temperatures and durations for some of the previously studied HEAs. Therefore, the as-cast ingots were homogenized at a selected temperature of 1200 °C for 2 h under an argon atmosphere to improve

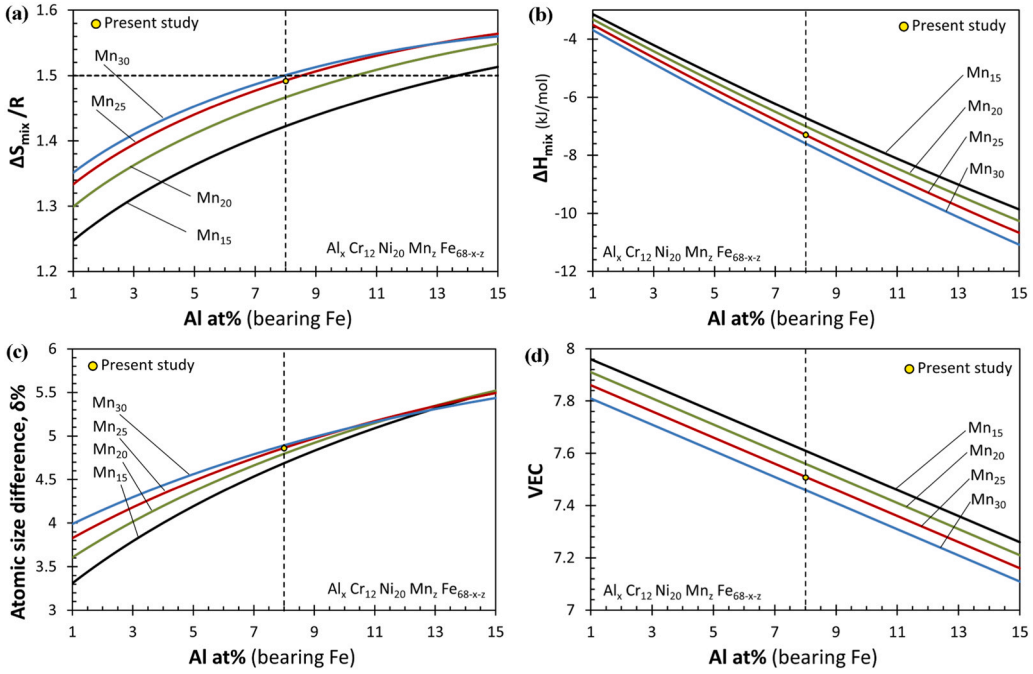

Fig. 1. Variation of thermodynamic parameters used in this study for HEA design, which shows the elemental effect of Mn and Al (a) ratio of mixing entropy ΔS_{mix} to the gas constant R, (b) mixing enthalpy ΔH_{mix} (kJ/mol), (c) atomic size difference δ%, and (d) valence electron concentration (VEC).

Table 3
Thermodynamic parameters for the current and previously studied HEAs.

Alloy	$Al_{10}Cr_{18}Mn_{21}Fe_{36}Ni_{15}$	$Al_5Cr_{12}Mn_{28}Fe_{35}Ni_{20}$	$Al_8Cr_{12}Mn_{25}Fe_{35}Ni_{20}$
Phases	FCC/B2	FCC	FCC
ΔH_{mix} *(kJ/mol)*	-7.37	-5.88	-7.30
ΔS_{mix} *(J/mol.K)*	12.63	12.06	12.41
ΔG_{mix} *(kJ/mol)*	-11.14	-9.47	-11
δ	5.04	4.54	4.86
Ω	2.94	3.51	2.88
T_m *(°K)*	1716	1713	1695
VEC	7.23	7.63	7.51
SSSI	-0.27	-0.20	-0.20
Δχ	0.133	0.143	0.141
ΔSmix /R	1.52	1.45	1.49
Ref.	[16]	[15]	Present work

Compositions in at%: mixing enthalpy (ΔH_{mix}), mixing entropy (ΔS_{mix}), Gibbs free energy of mixing (ΔG_{mix}), atomic size difference (δ), high-entropy phase formation factor (Ω), calculated melting temperature (T_m), valence electron concentration (VEC), SSSI, and electronegativity difference (Δχ)

the chemical homogeneity of the alloy and break down the dendritic structure. The ingots were then directly hot-rolled with a total reduction of ~50% in two passes, followed by water quenching.

2.3. Hot deformation schedule

Cylindrical samples of dimensions ∅6 × 8 mm were machined from the hot-rolled alloy with their axis parallel to the rolling direction. A uniaxial hot compression test was performed up to a true strain of 0.6 with a Gleeble 3800 thermo-mechanical simulator (Dynamic Systems Inc., Poestenkill, NY). A thermocouple was welded at the middle of the sample height to measure and control the temperature. Fig. 3 illustrates the typical thermomechanical cycles used in testing. The specimens were heated at a heating rate of 10 °C/s to the desired test temperatures (900, 1000, and 1100 °C). Isothermal soaking was performed for 60 s to eliminate any machining effect and dissolve any possible precipitation particles before deformation begins. After applying the single-hit compression at various strain rates (0.01, 0.1, 1, and 10 s^{-1}), the specimen was instantaneously fast-cooled at a cooling rate of 100 °C/s to preserve the high-temperature deformed structure. A Hydrawedge unit was employed for a high strain rate of 10 s^{-1} to precisely control the true strain and strain rate. As a reference sample for the initial microstructural study, the sample was directly cooled after isothermal soaking for 60 s without deformation.

2.4. Microstructure characterization

A field emission scanning electron microscope (FESEM JEOL JSM-7900 F) equipped with an Oxford electron backscatter diffraction (Oxford-EBSD) detector was utilized for direct microstructural investigation and dispersive X-ray spectroscopy (EDS). A 20 kV accelerating voltage and a step size of 0.05–0.2 μm were used during EBSD scans. Hot-rolled, pre-deformed, and hot-deformed microstructures were prepared for EBSD examination using a common preparation technique. The Fe-HEA sample was ground to 1200 grit, followed by polishing with a diamond suspension (diamond ≤ 3 μm). Electrolytic polishing was then used to remove any induced stress layers generated by mechanical grinding to obtain more accurate observations for the EBSD examination. Electropolishing was conducted with an electrolytic mixture of ~8% perchloric acid, ethanol,

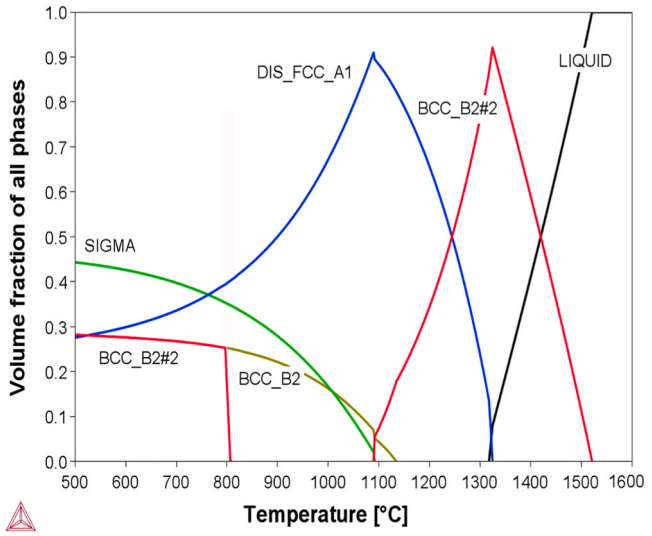

Fig. 2. Thermo-Calc for $Al_8Cr_{12}Mn_{25}Fe_{35}Ni_{20}$ HEA calculated using the TCHEA4 database.

Table 4
Nominal and chemical analysis of the Fe-HEA.

at%	Al	Cr	Mn	Fe	Ni
Nominal	8	12	25	35	20
XRF values	7.93	12.00	25.18	34.39	20.5

and distilled water at a voltage of 25 V for a period of 160–190 s at a subzero temperature.

X-ray diffraction (XRD) was carried out for phase analysis using a Rigaku SmartLab XRD equipped with a secondary beam monochromator diffractometer, utilizing Co-Kα radiation to reduce the fluorescence due to the high Mn and Fe content in the HEA. An electropolished specimen was examined using XRD at a scan speed of 1°/min and a step width of 0.05° for a scanning range (2θ) of 30–120°, operating at 40 kV and 135 mA. To determine the endothermic/exothermic phase transition and the melting point of the Fe-HEA, differential thermal analysis (DTA) was performed using a simultaneous thermal analyzer (NETZSCH STA 449 F3 Jupiter). The hot-rolled specimen of 7.14 mg was heated up to 1500 °C at a heating rate of 10 °C/min.

3. Results and discussion

3.1. Microstructure of hot-rolled material

A typical microstructure of the hot-rolled Fe-HEA investigated using EBSD analysis is shown in Fig. 4. The homogenization treatment and subsequent hot-rolling deformation significantly demoted

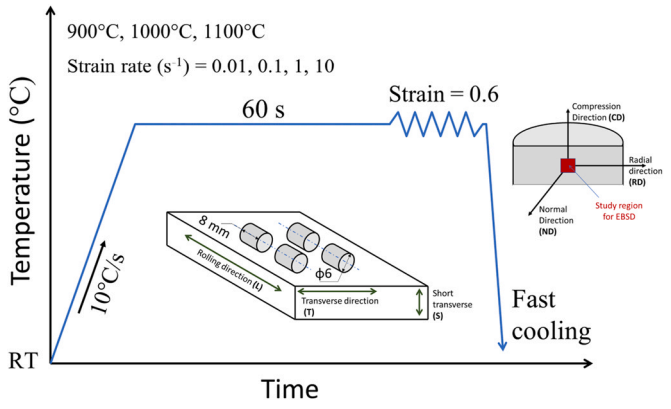

Fig. 3. Schematic diagram for the experimental thermo-mechanical schedule in the hot compression test for this study; middle insert depicts the sample size and orientation from the hot-rolled plate, and right insert depicts the schematic of the deformed sample sectioning showing the location of microstructural analysis region (red square).

the initial cast structure (i.e., columnar dendritic morphology), which commonly appears in as-cast HEAs [41,42] as a grain structure. The features of the hot-rolled grain structure, such as the grain and annealing boundaries, are clearly visible, as shown in Fig. 4(a). Lamella-like annealing twins with straight features dominate the microstructure, as evident in the inverse pole figure (IPF) map in Fig. 4(b). The corresponding grain size distribution is shown in Fig. 4(c), revealing an average grain size of 39 µm. From the disorientation angle distribution, the congruence analysis shows a strong correlation between the random pair and theoretical distribution, indicating a random texture in the hot-rolled structure, as shown in Fig. 4(d). In the same figure, the disorientation angle distribution of the neighbor pair greater than 50° is related to the annealed twin grains. Thus, the Fe-HEA could be classified as having low or intermediate stacking fault energy (SFE), which is in agreement with several previously studied FCC HEAs [43–45].

The XRD pattern of the hot-rolled structure is shown in Fig. 5(a), where all the peaks are indexed to the FCC structure. To determine the true value of the lattice parameter (a_o) of the FCC phase, the calculated value of the lattice parameter at each peak was extrapolated to $\sin^2\theta$, and the true value was estimated ($\sin^2\theta = 1$) [46], as shown in Fig. 5(b). The entire FCC structure was indexed to a lattice parameter of 0.36351 nm.

The Fe-HEA phase transition and melting range were measured via differential thermal analysis (DTA), as shown in Fig. 6. A notable peak was observed between 1014 °C and 1073 °C. This endothermic peak indicated a partial phase transformation from FCC to BCC/B2, as predicted by the Thermo-Calc phase diagram in Fig. 2. According to the isopleth equilibrium phase diagram for the HEA under consideration, the BCC/B2 phase is more thermodynamically stable than the FCC phase at temperatures greater than 1100 °C. The DTA peak

Table 5
Homogenization temperatures, homogenization time and experimentally determined phases observed for previously studied HEAs.

Alloy	Homog. Temp. (°C)	Homog. Time (h)	Phases present	Ref.
CrMnFeCoNi	1000	24	FCC (single-phase)	[35]
	1100	6	FCC (single-phase)	[36]
$Al_{0.5}CoCrFeNi$	1100	20	FCC + BCC (dual-phase)	[37]
$Al_{0.5}CoCrFeMnNi$	1000	6	FCC + B2	[38]
	1100		FCC (single-phase)	[38]
	1200		FCC (single-phase)	[38]
$Al_{0.7}CoCrFeMnNi$	1100	6	FCC + BCC (dual-phase)	[39]
$Fe_{22}Mn_{40}Ni_{30}Co_6Cr_2$	1200	2	FCC (single-phase)	[40]
$Fe_{32}Mn_{30}Ni_{30}Co_6Cr_2$	1200	2	FCC (single-phase)	[40]
$Fe_{42}Mn_{20}Ni_{30}Co_6Cr_2$	1200	2	FCC (single-phase)	[40]

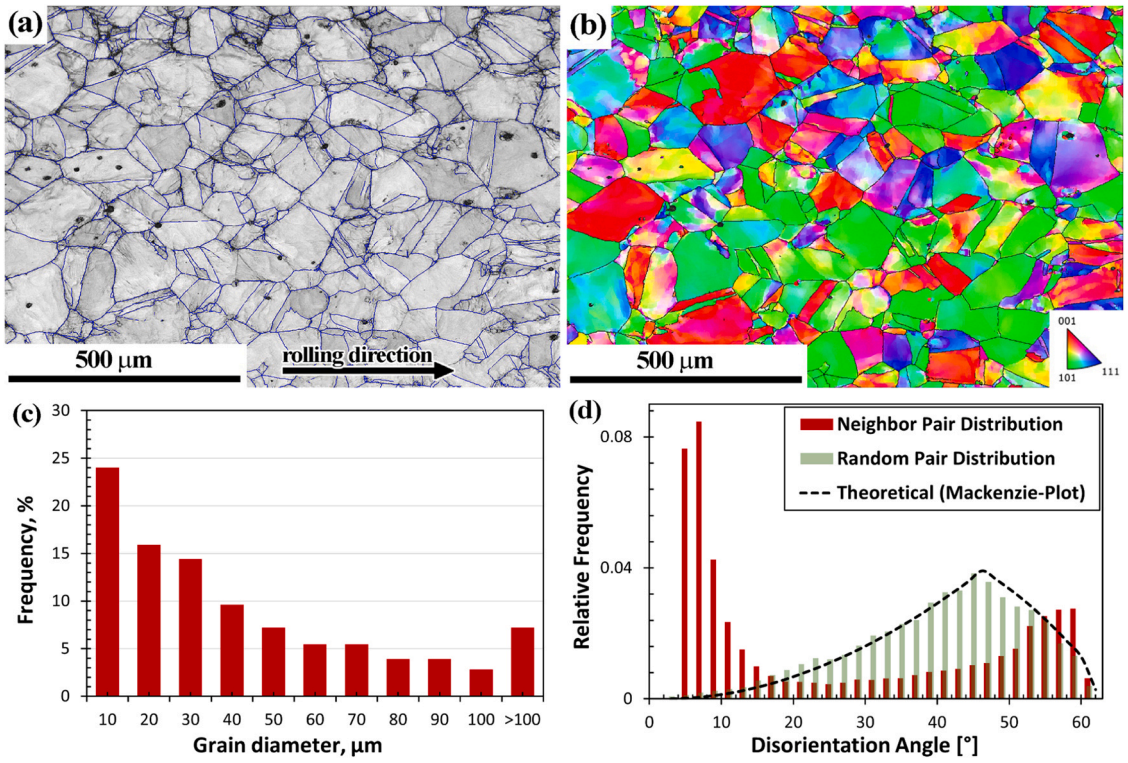

Fig. 4. EBSD of Fe-HEA after hot-rolling (a) SEM-EBSD band contrast (BC) image with high angle boundaries ˃ 15° in blue, (b) inverse pole figure (IPF) map of (a), (c) grain size distribution, and (d) disorientation angle distribution.

was observed at a temperature of 1333 °C, which signals the termination of melting. However, the onset of melting began at 1260 °C. The predicted melting point by the Thermo-Calc analysis was 1320 °C, which is in agreement with the DTA analysis.

3.2. Hot deformation behavior

The true stress-true strain curves of the isothermal compressive hot deformation tests of the Fe-HEA performed at different strain rates (0.01–10 s^{-1}) and various temperatures (900–1100ºC) are presented in Fig. 7. The flow-stress curves show a remarkable feature, which is that the flow stress decreases with increasing temperature at a constant strain rate. However, the Fe-HEA displayed a significant softening at low strain rates of 0.01–0.1 s^{-1} and high temperatures of 1000–1100 °C. The peak stresses were observed at these temperatures and strain rates. It is well known that the peak stress in the flow curve indicates the dynamic recrystallization (DRX) mechanism during hot deformation [47,48] that was observed for the flow curves

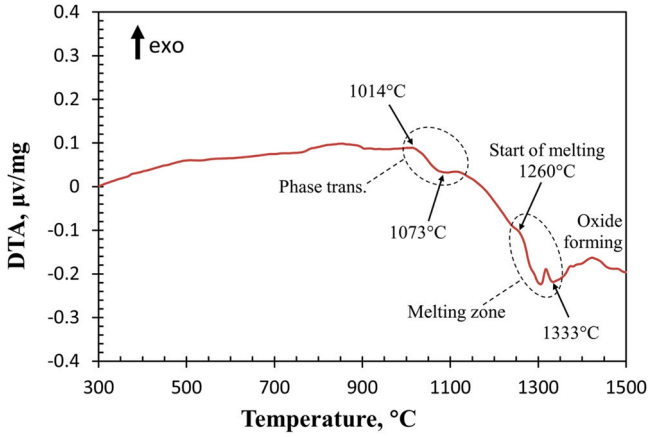

Fig. 6. Differential thermal analysis (DTA) of $Al_8Cr_{12}Mn_{25}Fe_{35}Ni_{20}$.

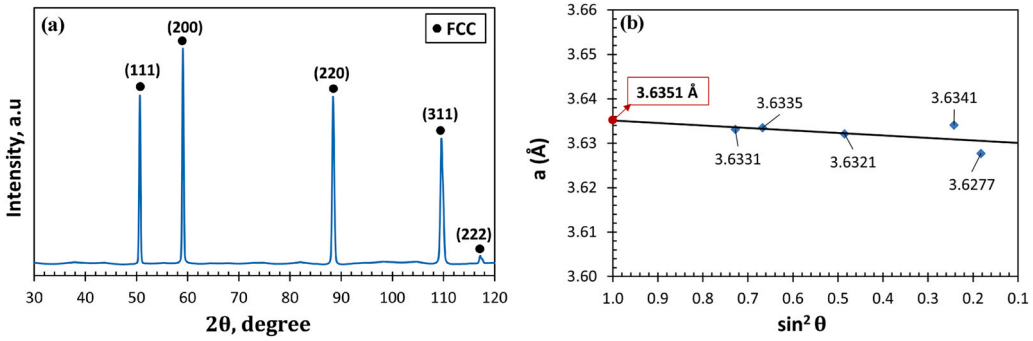

Fig. 5. XRD pattern of the studied Fe-HEA after hot-rolling at 1200 °C (a), and extrapolation to find the true value of the lattice parameter (b).

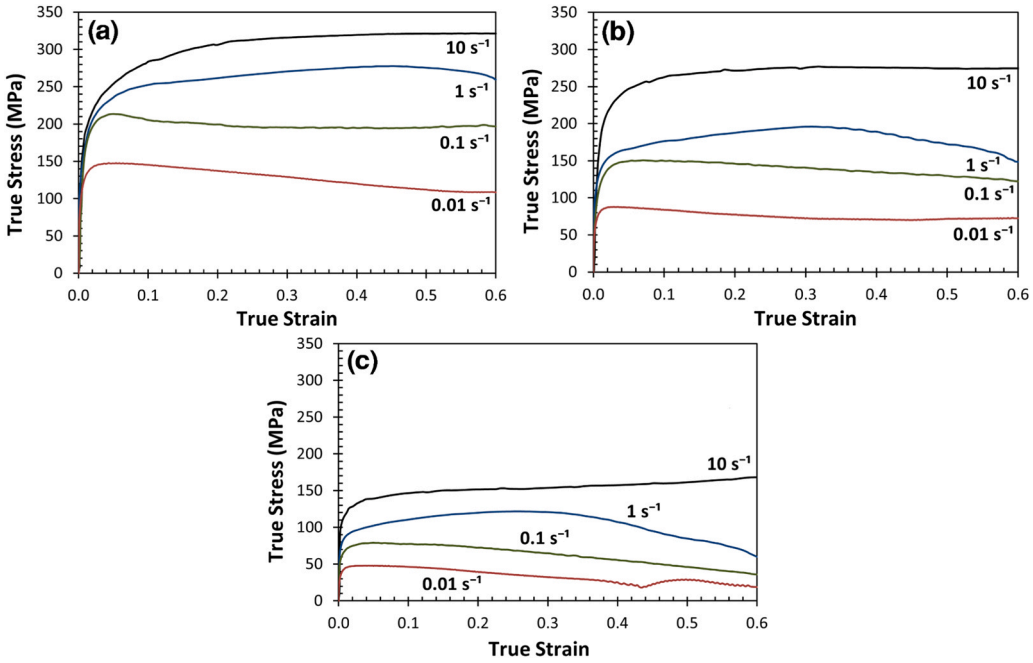

Fig. 7. Typical stress-strain curves of the hot compression tests for the $Al_8Cr_{12}Ni_{20}Mn_{25}Fe_{35}$ HEA at different strain rates at temperatures of (a) 900ºC, (b) 1000ºC and (c) 1100ºC.

of Fe-HEA at low strain rates of 0.01 and 0.1 s^{-1}. At a high strain rate (10 s^{-1}), the flow curves exhibit steady-state behavior after the initial hardening without exhibiting peak stress and a subsequent drop in the flow stress. A periodic modulation can be observed at a high temperature of 1100ºC and a low strain rate of 0.01 s^{-1}, which is indicative of similar hardening kinetics versus softening process for a strain higher than 0.4. In contrast, an increasing stress plateau was observed at a strain rate of 1 s^{-1} for all studied temperature ranges, followed by a gradual strain-softening mechanism at a strain value, which contrasted with the hot deformation temperature. At a high strain rate of 10 s^{-1}, steady-state flow was observed at low and medium temperatures. In contrast, a prevailing increase in the flow stress at a high strain was observed at a high temperature of 1100 °C (corresponding to ~0.8 T_m), which may be attributed to the increase in frictional force.

3.3. Constitutive flow stress relations

During hot deformation, the flow stress is influenced by the strain as well as both the deformation temperature and strain rate. The Zener-Hollomon parameter (Z) represents the relationship among the flow stress (σ), strain rate ($\dot{\varepsilon}$) and absolute temperature (T) in units of s^{-1}, where the flow stress is usually identified by the peak stress (σ_p), as reported by McQueen and Ryan [49], which can be expressed as follows:

$$Z = A[\sinh(\alpha\sigma_p)]^n = \dot{\varepsilon}\exp\left(\frac{Q_{HD}}{RT}\right) \quad (1)$$

where Q_{HD} is the activation energy for hot deformation, and R is the gas constant (8.314 $J.K^{-1}.mol^{-1}$). Furthermore, A, the stress multiplier (α), and the stress exponent (n) are material-related constants. Sellars and Tegrat [50] proposed the generally accepted Arrhenius hyperbolic sine relation, represented by Eq. (2), to correlate the strain rate (s^{-1}), flow stress (MPa), activation energy of hot deformation Q_{HD} ($kJ.mol^{-1}$), and absolute deformation temperature (K). This relation has been widely accepted in the hot deformation studies of several HEAs [24,51,52].

$$\dot{\varepsilon} = A[\sinh(\alpha\sigma)]^n \times \exp\left(-\frac{Q_{HD}}{RT}\right) \quad (2)$$

Different equations are used for different flow stress levels to correlate the hot deformation behavior of materials [53]. The following exponent equation expresses low-stress levels, where ασ < 0.8:

$$\dot{\varepsilon} = A\sigma^{n'} \times \exp\left(-\frac{Q_{HD}}{RT}\right) \quad (3)$$

while Eq. (4) is the power-exponent equation expressing high-stress levels (ασ > 1.2):

$$\dot{\varepsilon} = A\exp(\beta\ \ \sigma) \times \exp\left(-\frac{Q_{HD}}{RT}\right) \quad (4)$$

where n′ and β are material constants used to determine stress multiplier α using Eq. (5).

$$\alpha \approx \frac{\beta}{n'} \quad (5)$$

Provided that the peak stress (σ_p) is the point indicating DRX, the flow stress (σ) in the previous equations was identified as the peak stress (σ_p) in this study. For other conditions that did not exhibit a clear peak stress, σ_p was generally identified as the maximum flow stress. To determine the material constants, the natural logarithms of Eqs. (2), (3), and (4) are modified to Eqs. (6), (7), and (8), respectively.

$$\ln\dot{\varepsilon} = n\ \ \ln[\sinh(\alpha\sigma_p)] + \left[\ln A - \frac{Q_{HD}}{RT}\right] \quad (6)$$

$$\ln\dot{\varepsilon} = n'\ \ \ln\sigma_p + \left[\ln A - \frac{Q_{HD}}{RT}\right] \quad (7)$$

$$\ln\dot{\varepsilon} = \beta\sigma_p + \left[\ln A - \frac{Q_{HD}}{RT}\right] \quad (8)$$

The experimental true stress-true strain data were used to determine the material constants, as shown in Fig. 7. To calculate the stress multiplier (α), the material constants β and n′ were

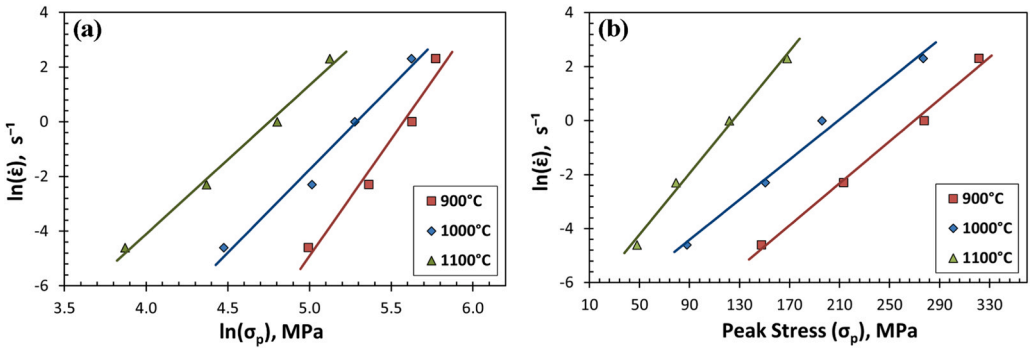

Fig. 8. Plots of linear fitting utilized to calculate n′ and β (a) $\ln\sigma_p$ vs $\ln\dot{\varepsilon}$ (b) σ_p vs $\ln\dot{\varepsilon}$; markers show the experimental data obtained from the peak stress (σ_p).

determined from the linear regression plots of $\ln\dot{\varepsilon}$ vs σ_p and $\ln\dot{\varepsilon}$ vs $\ln\sigma_p$, respectively, and Fig. 8 shows these results. The average values of β were 0.0443, and n′ was 6.6852; consequently, α was determined to be 0.00662.

Thus, the average stress exponent n was determined using Eq. (6) by plotting the linear fitting between $\ln\dot{\varepsilon}$ and $\ln[\sinh(\alpha\sigma_p)]$, as shown in Fig. 9(a), which was calculated to be 4.811. To calculate the activation energy of the hot deformation, Eq. (9) was determined by rearranging Eq. (6), and once again, the linear regression between $\frac{1}{T}$ and $\ln[\sinh(\alpha\sigma_p)]$ was plotted for each strain rate. Therefore, the Q_{HD} can be determined by ($\bar{S} \times 10Rn$), where $\bar{S}$ is the mean slope of the lines determined from Fig. 9(b) between (10^4/T) and $\ln[\sinh(\alpha\sigma_p)]$. Therefore, the Q_{HD} value of Fe-HEA was determined to be ~389.5 kJ/mol.

$$\ln[\sinh(\alpha\sigma_p)] = \left(\frac{Q_{HD}}{R\,n}\right)\left(\frac{1}{T}\right) + \frac{1}{n}[\ln\dot{\varepsilon} - \ln A] \quad (9)$$

The constant A in Eq. (1) can be calculated from the linear fitting plot between $\ln[\sinh(\alpha\sigma_p)]$ and ln(Z), as shown in Fig. 10 (a) and represented by Eq. (10).

$$\ln Z = \ln A + n\ln[\sinh(\alpha\sigma_p)] \quad (10)$$

Finally, the generalized Zener-Hollomon equation representing the correlation of all factors for the currently studied Fe-HEA is

$$Z = \dot{\varepsilon}\exp\left(\frac{389486}{R\,T}\right) = 1.0306 \times 10^{15}[\sinh(0.0066 \quad \sigma_p)]^{4.811} \quad (11)$$

Peak stresses were calculated using this equation to evaluate the accuracy of the proposed general Z-equation. Fig. 10 (b) shows the consistency of the model, with a high correlation coefficient of 99% between the calculated and experimental peak flow stress values.

Table 6 compares the Q_{HD} and stress exponent (n) values for Fe-HEA along with data from the literature for previously studied HEAs and high-manganese steel. This could be interpreted from the data, which shows that the Al and Mn content increased the Q_{HD} value. With Mn addition, the hot deformation activation energy increased dramatically from 301 to 434 kJ.mol^{-1} for the previously studied HEAs Al0.5CoCrFeNi (~11 at% Al) and $Al_{0.4}$MnCoCrFeNi (~7.4 at% Al and 18.5 at% Mn), respectively. The same effect of Mn on the activation energies was discussed by Li et al. [54] for austenitic steel, and by Mofarrehi et al. [55] for Al alloys. However, a study on twinning-induced plasticity (TWIP) steels with different Al content showed a proportional relationship between Al content and activation energy of hot deformation [56]. The same conclusion was confirmed when comparing the values of Q_{HD} from Table 6 for the HEAs CoCrFeMnNi and $Al_{0.4}$MnCoCrFeNi, where Al addition increased the Q_{HD} value. Thus, the relatively high Q_{HD} value of the HEA studied in this study could be related to the Al and Mn content.

3.4. Hot deformation microstructure evolution

The microstructural features of the hot-deformed specimens for selected conditions were investigated using EBSD. The indexing of EBSD patterns was ~98%, i.e., Kikuchi lines, which is an indicator for successful analysis [58]. The high-angle grain boundaries (HAGB) were identified (misorientation angle, θ > 15°) in blue lines, and alternatively, low-angle grain boundaries (LAGB) were represented by green lines (misorientation angles, 2° < θ < 15°). To investigate the initial microstructure prior to the hot deformation process (pre-deformation condition), the specimen was heated up to 1100 °C for 60 s and rapidly cooled to room temperature without any deformation. Fig. 11 (a) illustrates the band contrast image of the Fe-HEA for the pre-deformed condition, where the microstructure shows a structure close to that of the hot-rolled sample shown in Fig. 4(b). The structure indicates an almost coarse grain size, with approximately 65% of the grains less than 20 μm and 13% greater than 40 μm, as shown in Fig. 11 (c). The EBSD analysis confirmed the existence of a full FCC structure, confirming the XRD results previously mentioned

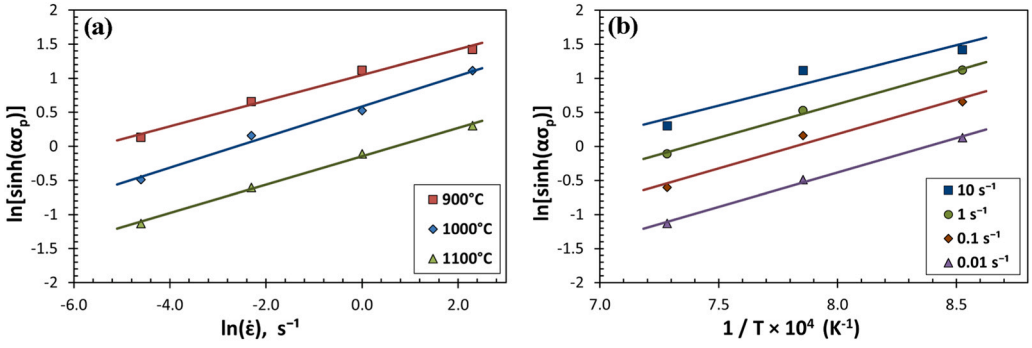

Fig. 9. Regression plot to calculate the stress exponent n from (a) relation between strain rate vs $\ln[\sinh(\alpha\sigma_p)]$, and the hot deformation activation energy Q_{HD} from (b) temperature dependance vs $\ln[\sinh(\alpha\sigma_p)]$.

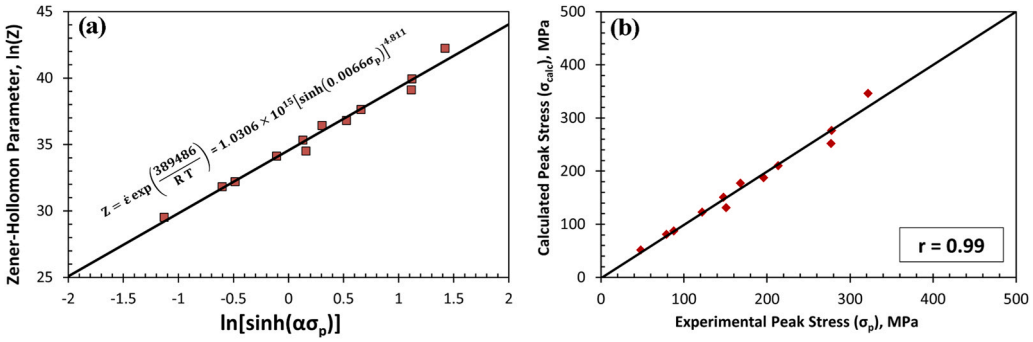

Fig. 10. Zener-Hollomon parameter (a) constructing the final constitutive equation showing the dependence of the peak flow stress on (lnZ), and (b) experimental vs calculated peak stresses using the constructed constitutive equation.

Table 6
Activation energy of compressive hot deformation and the stress exponent for the studied Fe-HEA compared with other HEAs and steels.

Alloy, at%	Q_{HD} (kJ.mol^{-1})	n	Ref.
$Al_8Cr_{12}Mn_{25}Fe_{35}Ni_{20}$	389.5	4.81	Present work
$Al_{0.5}CoCrFeNi$	301	6.05	[37]
CoCrFeMnNi	350	5.3	[24]
$Al_{0.4}MnCoCrFeNi$	434	6.86	[23]
AlCrCuFeNi	199	3.66	[57]
TWIP steel - $Fe_{bal.}Mn_{19}Al_{10}C_{2.6}V_{0.3}$	422	3.12	[56]

in Section 3.1. Fig. 11 (b) and (d) show the inverse pole figures (IPF) at high and low magnifications, respectively. The black arrows indicate that the annealing twins were confirmed to have different orientations than the parent grains. Annealing twins are a commonly observed feature in FCC metals and alloys [59], and Wang et al. [60] concluded a directly proportional relationship between the number of annealing twins and the amount of stored deformation energy.

Because it is a thermally activated diffusion-controlled process, DRX strongly depends on the rate of atom diffusion, migration of grain/sub-grain boundaries, and dislocation movements [61]. Fig. 12 (a) illustrates the microstructure of the Fe-HEA at 900 °C – 0.01 s^{-1} at a strain of 0.6 at low magnification. Horizontally-flattened grains were observed, which were assigned to the compressive strain in the vertical direction. A typical necklace structure was observed, with fine recrystallized grains along the initial grain boundaries. This suggests the activation of discontinuous dynamic recrystallization (DDRX) during hot deformation at the grain boundaries by the bulge mechanism stimulated by grain boundary migration [62,63]. This corresponds with the flow-curve behavior with a featured softening mechanism, shown in Fig. 7(a) and discussed in Section 3.2. LAGBs are generally observed in coarse flattened initial grains, as shown in Fig. 12 (b), which could be nucleation sites for DRX with further deformation [64]. The same distinct feature was reported by Hamada et al. [53] for medium-Mn stainless steel. The LAGBs inhomogeneous structure of the hot-deformed material can be

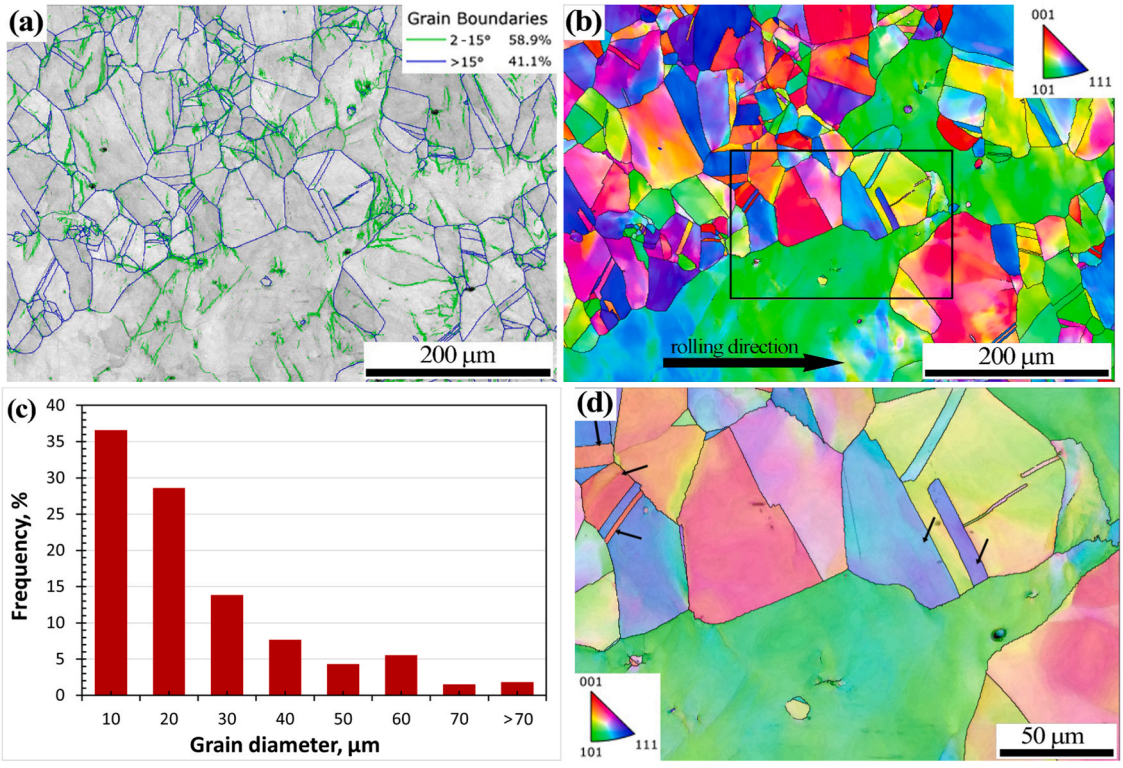

Fig. 11. Initial microstructure for the pre-deformed Fe-HEA specimen heated for 60 s at 1100 °C and fast cooled (a) SEM-EBSD band contrast map with low and high angle boundaries, (b) inverse pole figure (IPF) map of the selected area in (a), (c) distribution of grain size for the corresponding grains in (a), and (d) higher magnification of (b) with combined IPF and band contrast.

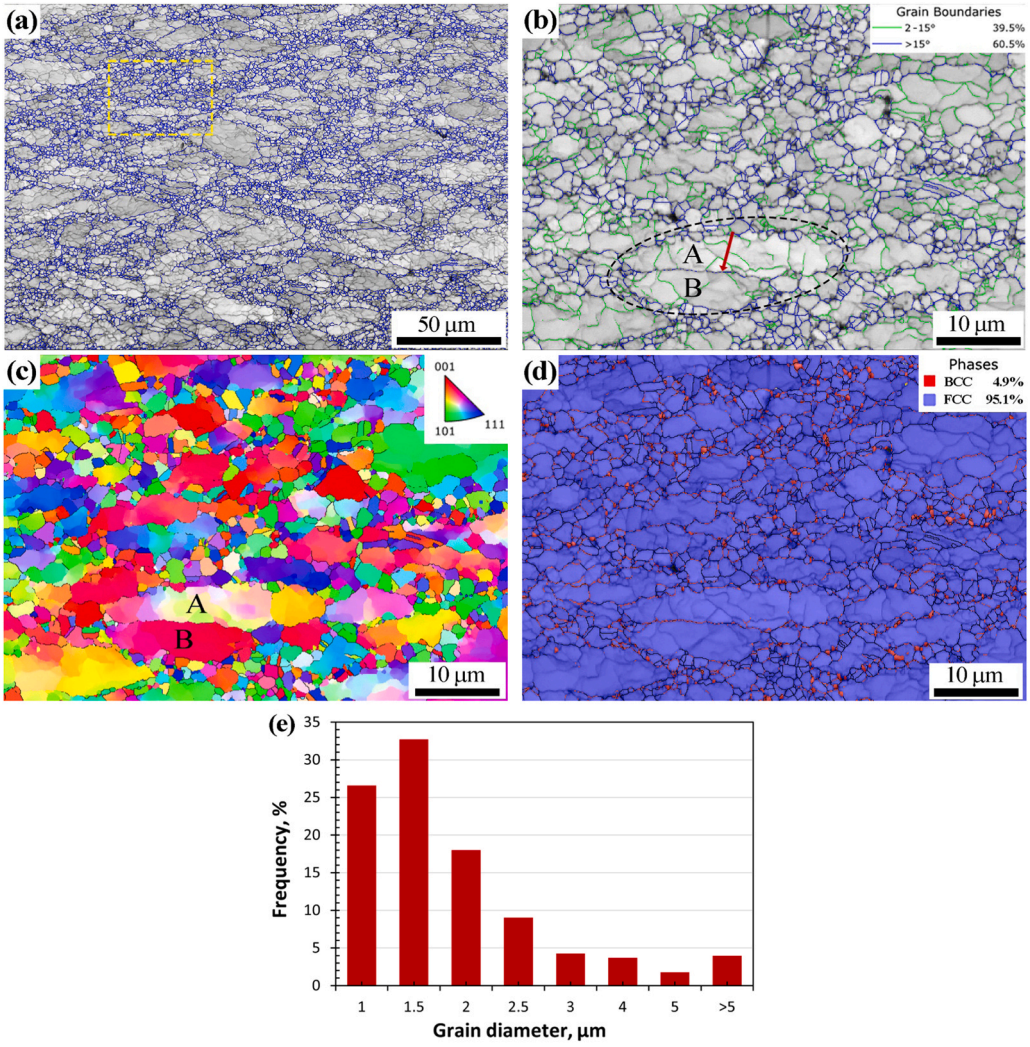

Fig. 12. Hot-deformed microstructure of Fe-HEA at 900 °C and 0.01 s^{-1} at a strain of 0.6 and compression axis in the vertical direction. (a) SEM-EBSD low-magnification band contrast (BC) image with high-angle boundaries ˃ 15° in blue, (b) high-magnification BC image with high/low-angle boundaries at the yellow rectangle site in (a), (c) high-magnification orientation map, (d) phase map of (b), and (d) equivalent grain diameter frequency distribution.

attributed to both the high dislocation density and local strain gradient. In the same figure, two neighboring coarse grains A and B are separated by HAGB, indicated by the red arrow. Moreover, from the orientation map shown in Fig. 12 (c), it can be observed that grain B has nearly the same orientation (001) along the inside LAGBs, whereas grain A has various orientations. This reveals that grain A probably underwent DRX with further deformation. The phase map in Fig. 12 (d) indicates the formation of the BCC/B2 phase at the grain boundaries of FCC grains, forming ~5% and highly observed at the HAGB (this phenomenon is discussed later in this section). The interpretation of the equivalent grain circle diameter distribution (Fig. 12 (e)) indicates that more than 77% of the total grains have a size of less than 2 µm, according to the interpreted grain size analysis shown in Fig. 12 (a).

The flow curve at a temperature of 1000 °C and strain rate 1 s^{-1} shows a peak stress at a strain of ~0.32, indicating a delay in the DRX and accumulation of dislocations, after which softening mechanism occurs. Fig. 13 (a) shows the low-magnification microstructure of the alloy after hot deformation under such conditions, where DRX progressed. Grains C and D in this figure are non-recrystallized large grains with no LAGBs observed inside. Such grains with specific orientations are slightly deformed and show only partial dynamic recovery, as indicated by the light gray contours inside these grains. Fig. 13 (b) and (e) indicate the DRX of the heavily deformed grains with HAGB fine grains shown in blue lines, which is enhanced because of the high accumulation of stored energy and dislocations in the first plateau. Micrograins with an average diameter of < 1 µm accounted for approximately 85% of the total grain count. The phase map is shown in Fig. 13 (d), indicating a 5% BCC/B2 structure in the DRX grains with HAGBs (discussed at the end of this section).

The microstructure at a high temperature of 1100 °C at 0.01 s^{-1} and 10 s^{-1} are shown in Fig. 14 and Fig. 15, respectively. The flow curve of the hot-deformed sample at a low strain rate (i.e., 0.01 s^{-1}) showed periodic modulation at a strain higher than 0.4. The orientation map shown in Fig. 14 (a) indicates dynamically recovered grains with the common planes of (001) and (101) in red and green, respectively. Relatively coarser grains of size < 10 µm form ~50% of the total grains owing to higher deformation temperatures and grain growth probability, as shown in Fig. 14 (c). A grain growth mechanism is expected under these conditions because of the low strain rate and high temperature, which allows the dislocation glide/climb mechanism. At a higher magnification, as shown in Fig. 14 (d), new DRX grains were observed inside the deformed grain. Phase map analysis revealed the same occurrences at lower deformation temperatures, where the BCC/B2 phase formed at the DRX grain boundaries. The BCC/B2 ratio was 1.5%, which could be assigned to the lower phase volume fraction at that temperature, as indicated by Themo-Calc (Fig. 2).

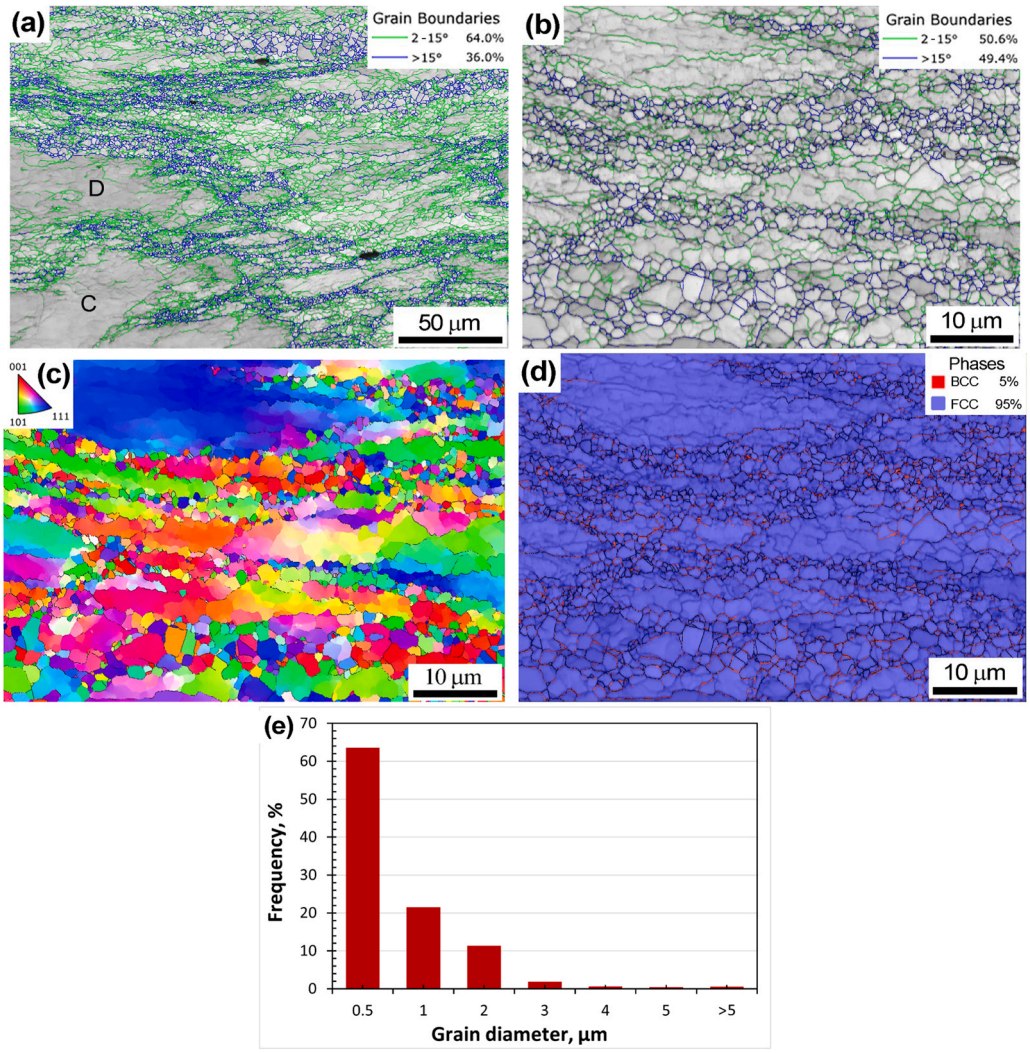

Fig. 13. EBSD of Fe-HEA at 1000 °C/1 s^{-1} at a strain of 0.6 (vertical compression axis).(a) low-magnification BC image, (b) high-magnification BC image, (c) high-magnification orientation map of (b), (d) phase map of (b), and (e) grain diameter frequency.

The flow curve at the same temperature of 1100 °C with a high strain rate of 10 s^{-1} showed a steady-state plateau. Fig. 15 (a) shows a partial DRX structure with coarse grains filled with LAGBs. Dislocation rearrangement is activated when the stresses reach a sufficiently high level, leading to a new strain-induced boundary or subboundary formation. At higher magnification, as shown in Fig. 15 (b), annealing twins can be observed within the HAGBs, indicated by blue lines. Xia et al. [65] linked the annealing twins within the DRX grains to the increased strain, which was promoted by grain boundary migration during DRX. In agreement with another study by Bozzol et al. [61], annealing twins were obtained by strain-induced boundary migration (SIBM). Relatively fine DRX grains can be observed, where fine grains (< 2 µm) form 47% of the total. Moreover, 37% of the grains measure between 2 and 6 µm. At the HAGBs, the previously observed BCC/B2 phase formation phenomena were observed, but with a lower fraction of 1.4%. The kernel average misorientation (KAM), shown in Fig. 15 (d), indicates that the local misorientation results from dislocations in the microstructure. The KAM map shows high misorientation/dislocations in the non-crystallized regions. The new fine DRX grains are promoted at the high strain rate of 10 s^{-1} and high temperature (1100 °C). This is attributed to the accumulation of sufficient dislocations and strain energy to maintain the DRX.

The precipitation of the BCC/B2 phase at the grain boundaries under different conditions could be attributed to the diffusional phase transformation. A previous study by Daniel et al. [66] on the precipitation kinetics of equiatomic CrMnFeCoNi alloy HEA revealed the same phenomenon of multiphase decomposition at the grain boundaries at elevated temperatures. The primary phase of a supersaturated solid solution contains destabilized supporting sites for heterogeneous nucleation and promotes diffusion at the grain boundaries, which provide nucleation sites and rapid diffusion pathways. Additionally, the previously discussed phase-fraction maps show that the BCC/B2 fraction (red) decreases with increasing hot deformation temperature. This could be related to the equilibrium phases shown in Fig. 2, where the BCC/B2 volume fraction varies with temperature, with a minimum amount at 1100 °C compared with the other temperatures at 900 and 1000 °C.

The high-magnification SEM image in Fig. 16 reveals the presence of this phase along the grain boundaries. The EDS maps show that the precipitated phase was enriched with Al and Ni, confirming the possibility of dynamic precipitation of the B2 phase. Patnamsetty et al. [44] reported the same phenomenon for $Al_{0.3}$CoCrFeNi, where B2 dynamic precipitation was caused by stimulated dynamic or static recrystallization. Moreover, it was discussed that the Al-Ni rich B2 precipitates might act as particle-stimulated nucleation (PSN)

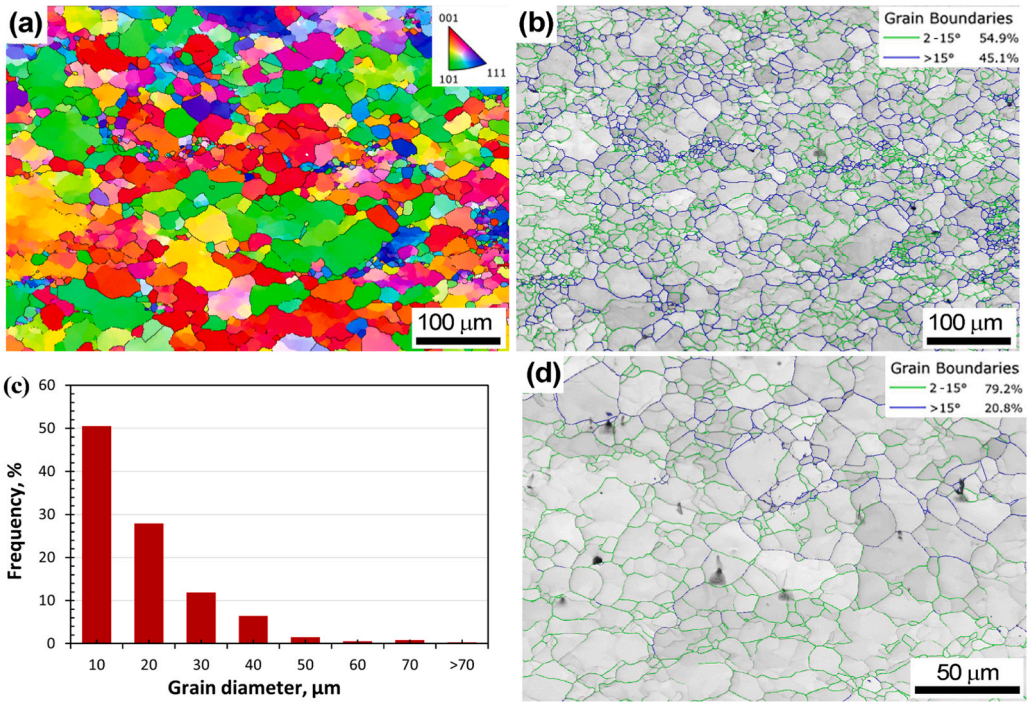

Fig. 14. EBSD of Fe-HEA at 1100 °C/0.01 s^{-1} at a strain of 0.6 (vertical compression axis). (a) low-magnification IPF map, (b) boundary-map of (a), (c) grain size distribution diameter, and (d) high-magnification boundary-map,.

sites for new recrystallized grains along with the existence of a substructure. However, it is difficult to confirm the PSN mechanism in the current study because the B2 phase exists at high temperatures, as indicated from the equilibrium phase diagram as in the case of hot-deformed samples at 900 °C/0.01 s^{-1} and 1000 °C/1 s^{-1}, which requires further investigation. In another study, Li et al. [67] reported that elemental segregation has a higher tendency at HAGBs of higher misorientation owing to the higher driving force for segregation. On

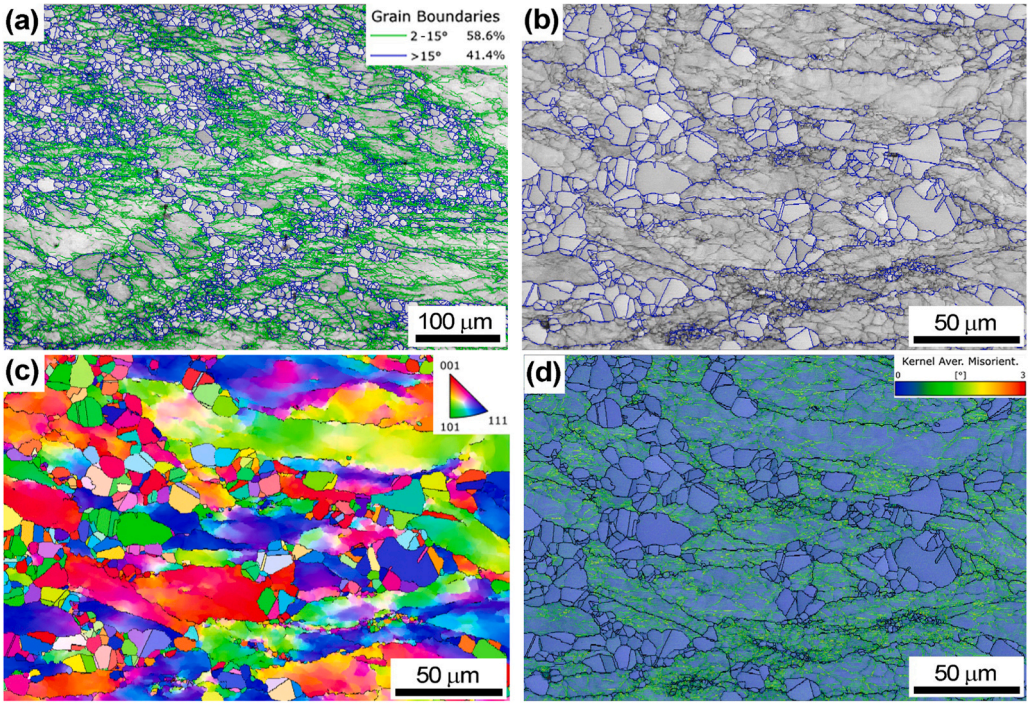

Fig. 15. Hot-deformed microstructure of Fe-HEA at 1100 °C/10 s^{-1} at a strain of 0.6 (a) SEM-EBSD band contrast image, (b) high-magnification band contrast of (a) showing HAGBs higher than 15° in blue lines, (c) IPF map of (b), (c) kernel average misorientation (KAM) map.

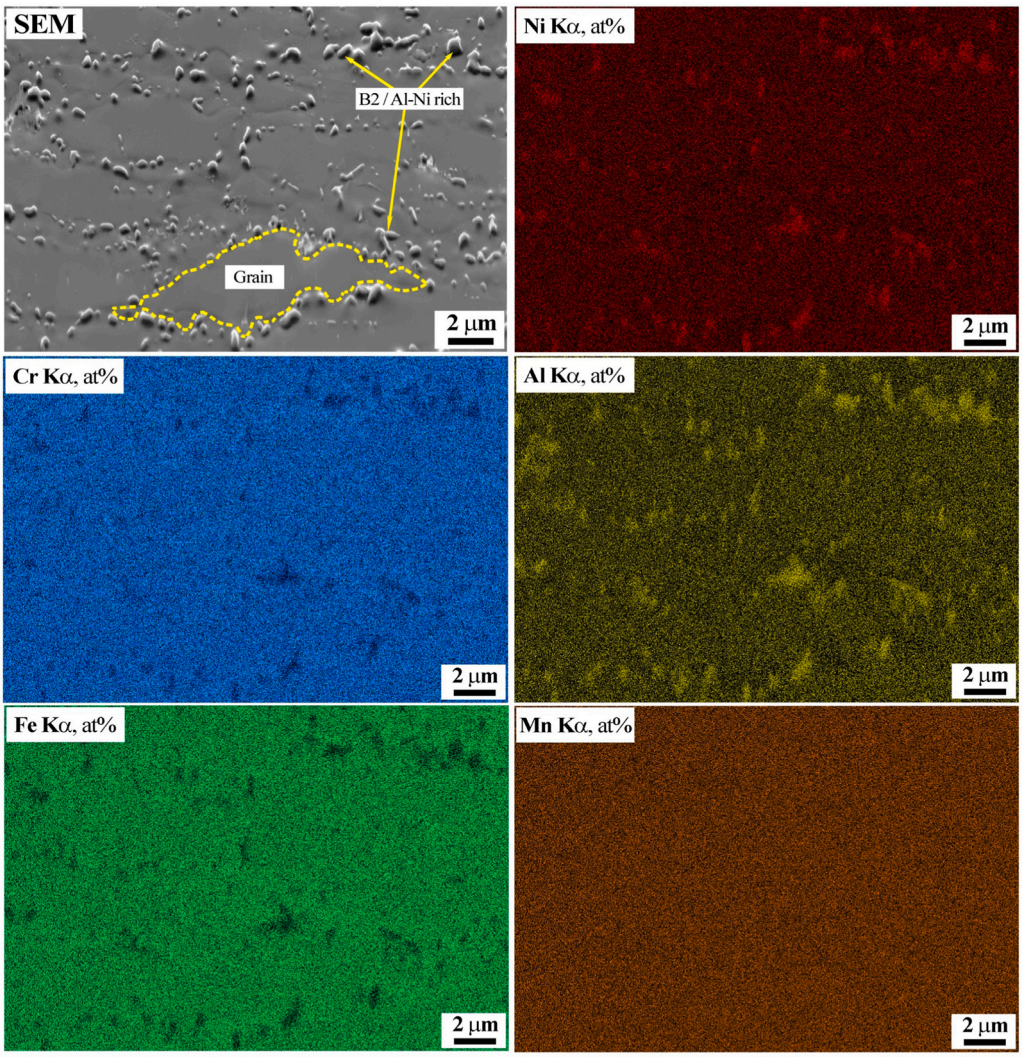

Fig. 16. SEM image and elemental distribution map of hot-deformed Fe-HEA at 900 °C/0.01 s^{-1}.

the other hand, the tendency of Al and Ni segregation in Fe-HEA is related to the high tendency to mix ($\Delta H_{Al\text{-}Ni}$ = −22 kJ/mol), which is the highest among all values shown in Table 2.

4. Conclusion

Hot-compression tests utilizing the Gleeble 3800 thermo-mechanical simulator were conducted to examine the hot-deformation behavior of the newly developed cost-effective HEA, $Al_8Cr_{12}Mn_{25}Fe_{35}Ni_{20}$ (Fe-HEA). The hot deformation tests were performed at different temperatures (900–1100 °C) and strain rates (0.01–10 s^{-1}), and the microstructure evolution was studied using SEM-EBSD for selective conditions. The main conclusions of this study are as follows:

i. The hot-rolled alloy showed a complete FCC structure at room temperature, as confirmed by the XRD and EBSD analyses. A successful homogenization and processing regime was implemented with a final homogenized structure and mostly equiaxed grains.
ii. The flow curves were sensitive to the deformation temperatures and strain rates. Microstructural examination confirmed the dynamic recrystallization mechanism under all deformation conditions.
iii. The calculated activation energy for Fe-HEA was 389.5 kJ.mol^{-1}, and this value was attributed to its relatively high Al and Mn content.
iv. Constitutive equations for the peak flow stress of hot-deformed Fe-HEA at various temperatures and strain rates were successfully implemented. The final model exhibited a high correlation (0.99) between the experimental and calculated values. The correlations among the strain rate, peak stress, and deformation temperature are as follows:

$$\dot{\varepsilon}=1.0306\times10^{15}[\sinh(0.0066\sigma_p)]^{4.811}\times\exp\left(\frac{-389486}{RT}\right)$$

v. The microstructural examination of hot-deformed conditions indicated that DRX initiated at the grain boundaries and necklace structure was observed at 900 °C/0.01 s^{-1}. At a high testing temperature (1100 °C) and high strain rate (10 s^{-1}), annealing twins were observed in the fully recrystallized grains derived by SIBM.
vi. Al-Ni-rich B2 precipitates induced by diffusional phase transformation were observed at the DRX grain boundaries under

different hot deformation conditions, which was confirmed by EDS mapping.

CRediT authorship contribution statement

Ahmed W. Abdelghany: Conceptualization, Methodology, Investigation, Writing – original draft, Formal analysis. **Matias Jaskari:** Conducting SEM-EBSD examination, Investigation. **Atef S. Hamada:** Conceptualization, Methodology, Writing – review & editing. **Antti Järvenpää:** Funding acquisition. **Hassan A. El-Hofy:** Supervision. **Akihiko Chiba:** Supervision. **Mohamed Abdel-Hady Gepreel:** Conceptualization, Supervision, Writing – review & editing.

Data Availability

No data was used for the research described in the article.

Declaration of Competing Interest

The authors declare that they have no known competing financial interests or personal relationships that could have appeared to influence the work reported in this paper.

Acknowledgments

Future Manufacturing Technologies (FMT) research group, Kerttu Saalasti Institute, University of Oulu is acknowledged for funding the experimental work of this study. This work was partially supported by the Grants-in-Aid for Scientific Research (KAKENHI, grant number: 18H05455) from the Japan Society for the Promotion of Science, and the Central Department of Missions (CDM) under the Cultural Affairs and Missions Sector at the Ministry of Higher Education of Egypt (MoHE).

References

[1] P.L.J. Conway, T.P.C. Klaver, J. Steggo, E. Ghassemali, High entropy alloys towards industrial applications: high-throughput screening and experimental investigation, Mater. Sci. Eng. A 830 (2022) 142297, https://doi.org/10.1016/j.msea.2021.142297

[2] Y. Fu, X. Wang, W. Guo, High-entropy alloys: emerging materials for advanced functional applications, (2021). https://doi.org/10.1039/d0ta09601f.

[3] Z. Liu, Z. Xiong, K. Chen, X. Cheng, Large-size high-strength and high-ductility AlCoCrFeNi2.1 eutectic high-entropy alloy produced by hot-rolling and subsequent aging, Mater. Lett. 315 (2022), https://doi.org/10.1016/J.MATLET.2022.131933

[4] S.W. Wu, G. Wang, Y.D. Jia, J. Yi, Q.J. Zhai, C.T. Liu, B.A. Sun, H.J. Chu, J. Shen, P.K. Liaw, T.Y. Zhang, Enhancement of strength-ductility trade-off in a high-entropy alloy through a heterogeneous structure, Acta Mater. 165 (2019) 444–458, https://doi.org/10.1016/j.actamat.2018.12.012

[5] J. Chen, X. Zhou, W. Wang, B. Liu, Y. Lv, W. Yang, D. Xu, Y. Liu, A review on fundamental of high entropy alloys with promising high–temperature properties, J. Alloy. Compd. 760 (2018) 15–30, https://doi.org/10.1016/j.jallcom.2018.05.067

[6] D. Raabe, C.C. Tasan, H. Springer, M. Bausch, From high-entropy alloys to high-entropy steels, Steel Res. Int. 86 (2015) 1127–1138, https://doi.org/10.1002/srin.201500133

[7] A. Kumar, A. Singh, A. Suhane, Mechanically alloyed high entropy alloys: existing challenges and opportunities, J. Mater. Res. Technol. 17 (2022) 2431–2456, https://doi.org/10.1016/j.jmrt.2022.01.141

[8] Y. Iijima, T. Nagase, A. Matsugaki, P. Wang, K. Ameyama, T. Nakano, Design and development of Ti–Zr–Hf–Nb–Ta–Mo high-entropy alloys for metallic biomaterials, Mater. Des. 202 (2021), https://doi.org/10.1016/J.MATDES.2021.109548

[9] A.H. Awad, H.A. El-Hofy, A. Chiba, M.A.-H. Gepreel, Robust mechanical properties and corrosion resistance of new low-cost hot-forged and aged -type Ti–14Mn–(x)Zr alloys, J. Alloy. Compd. 904 (2022) 164098, https://doi.org/10.1016/J.JALLCOM.2022.164098

[10] A.J.S.F. Tapia, D. Yim, H.S. Kim, B.J. Lee, An approach for screening single phase high-entropy alloys using an in-house thermodynamic database, Intermetallics 101 (2018) 56–63, https://doi.org/10.1016/j.intermet.2018.07.009

[11] S. Gorsse, M.H. Nguyen, O.N. Senkov, D.B. Miracle, Database on the mechanical properties of high entropy alloys and complex concentrated alloys, Data Br. 21 (2018) 2664–2678, https://doi.org/10.1016/j.dib.2018.11.111

[12] L. Qiao, Y. Liu, J. Zhu, A focused review on machine learning aided high-throughput methods in high entropy alloy, J. Alloy. Compd. 877 (2021) 160295, https://doi.org/10.1016/j.jallcom.2021.160295

[13] X. Fu, C.A. Schuh, E.A. Olivetti, Materials selection considerations for high entropy alloys, Scr. Mater. 138 (2017) 145–150, https://doi.org/10.1016/J.SCRIPTAMAT.2017.03.014

[14] S. Elkatatny, M.A.H. Gepreel, A. Hamada, K. Nakamura, K. Yamanaka, A. Chiba, Effect of Al content and cold rolling on the microstructure and mechanical properties of Al5Cr12Fe35Mn28Ni20 high-entropy alloy, Mater. Sci. Eng. A 759 (2019) 380–390, https://doi.org/10.1016/j.msea.2019.05.056

[15] D.G. Shaysultanov, G.A. Salishchev, Y.V. Ivanisenko, S.V. Zherebtsov, M.A. Tikhonovsky, N.D. Stepanov, Novel Fe36Mn21Cr18Ni15Al10high entropy alloy with bcc/B2 dual-phase structure, J. Alloy. Compd. 705 (2017) 756–763, https://doi.org/10.1016/j.jallcom.2017.02.211

[16] T. Nguyen, M. Huang, H. Li, L. Hong, S. Yang, Effect of Al content on microstructure and mechanical properties of as-cast AlxFeMnNiCrCu0.5 high-entropy alloys, Mater. Sci. Eng. A. 832 (2022), https://doi.org/10.1016/J.MSEA.2021.142495

[17] M. Asadikiya, S. Yang, Y. Zhang, C. Lemay, D. Apelian, Y. Zhong, A review of the design of high-entropy aluminum alloys: a pathway for novel Al alloys, J. Mater. Sci. 56 (2021) 12093–12110, https://doi.org/10.1007/s10853-021-06042-6

[18] M. Ogura, T. Fukushima, R. Zeller, P.H. Dederichs, Structure of the high-entropy alloy AlxCrFeCoNi: Fcc versus bcc, J. Alloy. Compd. 715 (2017) 454–459, https://doi.org/10.1016/j.jallcom.2017.04.318

[19] C. Haase, L.A. Barrales-Mora, From high-manganese steels to advanced high-entropy alloys, Metals 9 (2019), https://doi.org/10.3390/met9070726

[20] A. Khosravifard, A. Hamada, A. Järvenpää, P. Karjalainen, Enhancement of grain structure and mechanical properties of a high-Mn twinning-induced plasticity steel bearing Al–Si by fast-heating annealing, Mater. Sci. Eng. A 795 (2020) 139949, https://doi.org/10.1016/j.msea.2020.139949

[21] W. Bleck, C. Haase, Physical metallurgy of high manganese steels, 2019. https://doi.org/10.3390/met9101053.

[22] M. Annasamy, N. Haghdadi, A. Taylor, P. Hodgson, D. Fabijanic, Dynamic recrystallization behaviour of AlxCoCrFeNi high entropy alloys during high-temperature plane strain compression, Mater. Sci. Eng. A 745 (2019) 90–106, https://doi.org/10.1016/J.MSEA.2018.12.102

[23] H. Kaypour, S. Nategh, R. Gholamipour, A. Khodabandeh, High-temperature compressive behavior and kinetics analysis of Al 0.4 MnCrCoFeNi high entropy alloy, (2021). https://doi.org/10.1088/2053–1591/ac045c.

[24] R.R. Eleti, T. Bhattacharjee, L. Zhao, P.P. Bhattacharjee, N. Tsuji, Hot deformation behavior of CoCrFeMnNi FCC high entropy alloy, Mater. Chem. Phys. 210 (2018) 176–186, https://doi.org/10.1016/J.MATCHEMPHYS.2017.06.062

[25] Q. Tian, G. Zhang, K. Yin, L. Wang, W. Wang, W. Cheng, Y. Wang, J.C. Huang, High temperature deformation mechanism and microstructural evolution of relatively lightweight AlCoCrFeNi high entropy alloy, Intermetallics 119 (2020) 106707, https://doi.org/10.1016/j.intermet.2020.106707

[26] S. Yang, G. Liu, Y. Zhong, Revisit the VEC criterion in high entropy alloys (HEAs) with high-throughput ab initio calculations: a case study with Al-Co-Cr-Fe-Ni system, J. Alloy. Compd. 916 (2022) 165477, https://doi.org/10.1016/J.JALLCOM.2022.165477

[27] S.A. Kube, S. Sohn, D. Uhl, A. Datye, A. Mehta, J. Schroers, Phase selection motifs in High Entropy Alloys revealed through combinatorial methods: large atomic size difference favors BCC over FCC, Acta Mater. 166 (2019) 677–686, https://doi.org/10.1016/j.actamat.2019.01.023

[28] X. Yang, Y. Zhang, Prediction of high-entropy stabilized solid-solution in multi-component alloys, Mater. Chem. Phys. 132 (2012) 233–238, https://doi.org/10.1016/j.matchemphys.2011.11.021

[29] S. Guo, C.T. Liu, Phase stability in high entropy alloys: formation of solid-solution phase or amorphous phase, Prog. Nat. Sci. Mater. Int 21 (2011) 433–446, https://doi.org/10.1016/S1002-0071(12)60080-X

[30] D.B. Miracle, O.N. Senkov, A critical review of high entropy alloys and related concepts, Acta Mater. 122 (2017) 448–511, https://doi.org/10.1016/j.actamat.2016.08.081

[31] H. Gasan, A. Ozcan, New eutectic high-entropy alloys based on Co–Cr–Fe–Mo–Ni–Al: design, characterization and mechanical properties, Met. Mater. Int. 26 (2020) 1152–1167, https://doi.org/10.1007/s12540-019-00515-9

[32] C. Colinet, Comparison of enthalpies of formation and enthalpies of mixing in transition metal based alloys, Thermochim. Acta 314 (1998) 229–245, https://doi.org/10.1016/S0040-6031(98)00238-X

[33] A. Takeuchi, A. Inoue, Mixing enthalpy of liquid phase calculated by miedema's scheme and approximated with sub-regular solution model for assessing forming ability of amorphous and glassy alloys, Intermetallics 18 (2010) 1779–1789, https://doi.org/10.1016/j.intermet.2010.06.003

[34] Z. Li, D. Raabe, Strong and ductile non-equiatomic high-entropy alloys: design, processing, microstructure, and mechanical properties, Jom 69 (2017) 2099–2106, https://doi.org/10.1007/s11837-017-2540-2

[35] M. Ji, S. Praveen, H. Je, J. Wung, J. Moon, H. Seop, High-temperature tensile deformation behavior of hot rolled CrMnFeCoNi high-entropy alloy, J. Alloy. Compd. 730 (2018) 242–248, https://doi.org/10.1016/j.jallcom.2017.09.293

[36] H.T. Jeong, H.K. Park, K. Park, T.W. Na, W.J. Kim, High-temperature deformation mechanisms and processing maps of equiatomic CoCrFeMnNi high-entropy alloy, Mater. Sci. Eng. A 756 (2019) 528–537, https://doi.org/10.1016/J.MSEA.2019.04.057

[37] Y. Zhang, J. Li, J. Wang, S. Niu, H. Kou, Hot deformation behavior of as-cast and homogenized Al0.5CoCrFeNi high entropy alloys, Metals 6 (2016), https://doi.org/10.3390/met6110277

[38] J. Moon, J.W. Bae, M.J. Jang, M. Baek, D. Yim, B.-J. Lee, S. Kim, Effects of homogenization temperature on cracking during cold-rolling of Al 0.5 CoCrFeMnNi high-entropy alloy, (2017). https://doi.org/10.1016/j.matchemphys.2017.06.043.
[39] H.T. Jeong, H.K. Park, W.J. Kim, Dynamic recrystallization and hot deformation mechanisms of a eutectic Al0.7CoCrFeMnNi high-entropy alloy, J. Alloy. Compd. 871 (2021), https://doi.org/10.1016/J.JALLCOM.2021.159488
[40] D. Ma, M. Yao, K.G. Pradeep, C.C. Tasan, H. Springer, D. Raabe, Phase stability of non-equiatomic CoCrFeMnNi high entropy alloys, Acta Mater. 98 (2015) 288–296, https://doi.org/10.1016/j.actamat.2015.07.030
[41] J.T. Fan, L.J. Zhang, P.F. Yu, M.D. Zhang, G. Li, P.K. Liaw, R.P. Liu, A novel high-entropy alloy with a dendrite-composite microstructure and remarkable compression performance, Scr. Mater. 159 (2019) 18–23, https://doi.org/10.1016/j.scriptamat.2018.09.008
[42] A.W. Abdel-Ghany, S. Elkatatny, M.A.H. Gepreel, Microstructure and mechanical properties investigation of new al10cr12mn28fe(50-x)ni(x) high entropy alloys, Mater. Sci. Forum, 998 MSF (2020) 9–14, https://doi.org/10.4028/www.scientific.net/MSF.998.9
[43] Z. Li, S. Zhao, H. Diao, P.K. Liaw, M.A. Meyers, High-velocity deformation of Remarkable resistance to shear failure, (2017) 1–8. https://doi.org/10.1038/srep42742.
[44] M. Patnamsetty, S. Ghosh, M.C. Somani, P. Peura, Characterization of hot deformation behavior of Al0.3CoCrFeNi high-entropy alloy and development of processing map, J. Alloy. Compd. 914 (2022) 165341, https://doi.org/10.1016/j.jallcom.2022.165341
[45] B. Grabowski, Z. Li, K. Fritz, Ab initio assisted design of quinary dual-phase high-entropy alloys with transformation-induced plasticity, Acta Mater. 136 (2017) 262–270, https://doi.org/10.1016/j.actamat.2017.07.023
[46] Y. Waseda, E. Matsubara, K. Shinoda, X-Ray Diffraction Crystallography, Springer Berlin Heidelberg, 2011, https://doi.org/10.1007/978-3-642-16635-8
[47] J.J. Jonas, X. Quelennec, L. Jiang, É. Martin, The Avrami kinetics of dynamic recrystallization, Acta Mater. 57 (2009) 2748–2756, https://doi.org/10.1016/J.ACTAMAT.2009.02.033
[48] G.E. Dieter, H.A. Kuhn, S.L. Semiatin, Handbook of Workability and Process Design, (2003). www.asminternational.org.
[49] H.J. McQueen, N.D. Ryan, Constitutive analysis in hot working, Mater. Sci. Eng. A 322 (2002) 43–63, https://doi.org/10.1016/S0921-5093(01)01117-0
[50] C.M. Sellars, W.J.M. Tegart, Hot Workability, Http://Dx.Doi.Org/10.1179/Imtlr.1972.17.1.1. 17 (2013) 1–24. https://doi.org/10.1179/IMTLR.1972.17.1.1.
[51] N. Nayan, G. Singh, S.V.S.N. Murty, A.K. Jha, B. Pant, K.M. George, U. Ramamurty, Hot deformation behaviour and microstructure control in AlCrCuNiFeCo high entropy alloy, Intermetallics 55 (2014) 145–153, https://doi.org/10.1016/J.INTERMET.2014.07.019
[52] Z. Savaedi, R. Motallebi, H. Mirzadeh, A review of hot deformation behavior and constitutive models to predict flow stress of high-entropy alloys, J. Alloy. Compd. 903 (2022), https://doi.org/10.1016/J.JALLCOM.2022.163964
[53] A. Hamada, T. Juuti, A. Khosravifard, A. Kisko, P. Karjalainen, D. Porter, J. Kömi, Effect of silicon on the hot deformation behavior of microalloyed TWIP-type stainless steels, Mater. Des. 154 (2018) 117–129, https://doi.org/10.1016/J.MATDES.2018.05.029
[54] D. Li, Y. Feng, F. Shangguan, W. Zhao, Q. Liu, K. Wang, Influences of manganese on the hot deformation of austenitic fe-mn-si-al alloys, Rev. Adv. Mater. Sci. 33 (2013) 342–347.
[55] M. Mofarrehi, M. Javidani, X. Chen, Effect of Mn content on the hot deformation behavior and microstructure evolution of Al – Mg – Mn 5xxx alloys, Mater. Sci. Eng. A. 845 (2022) 143217, https://doi.org/10.1016/j.msea.2022.143217
[56] A. Hamada, A. Khosravifard, D. Porter, L. Pentti Karjalainen, Physically based modeling and characterization of hot deformation behavior of twinning-induced plasticity steels bearing vanadium and niobium, Mater. Sci. Eng. A 703 (2017) 85–96, https://doi.org/10.1016/J.MSEA.2017.07.038
[57] X. Wang, Y. Zhang, X. Ma, High temperature deformation and dynamic recrystallization behavior of AlCrCuFeNi high entropy alloy, Mater. Sci. Eng. A 778 (2020) 139077, https://doi.org/10.1016/j.msea.2020.139077
[58] S.I. Wright, M.M. Nowell, S.P. Lindeman, P.P. Camus, M. De Graef, M.A. Jackson, Introduction and comparison of new EBSD post-processing methodologies, Ultramicroscopy 159 (2015) 81–94, https://doi.org/10.1016/J.ULTRAMIC.2015.08.001
[59] C. Li, B. Ma, Y. Song, K. Li, J. Dong, The annealing twins of Fe-20Mn-4Al-0.3C austenitic steels during symmetric and asymmetric hot rolling, Metals 8 (2018) 1–10, https://doi.org/10.3390/met8110882
[60] W. Wang, S. Lartigue-Korinek, F. Brisset, A.L. Helbert, J. Bourgon, T. Baudin, Formation of annealing twins during primary recrystallization of two low stacking fault energy Ni-based alloys, J. Mater. Sci. 50 (2015) 2167–2177, https://doi.org/10.1007/s10853-014-8780-4
[61] A. Rollett, F. Humphreys, G.S. Rohrer, M. Hatherly, Recrystallization and Related Annealing Phenomena, second ed., Elsevier Ltd, 2004, https://doi.org/10.1016/B978-0-08-044164-1.X5000-2
[62] X. Zhong, L. Huang, F. Liu, Discontinuous Dynamic Recrystallization Mechanism and Twinning Evolution during Hot Deformation of Incoloy 825, J. Mater. Eng. Perform. 29 (n.d.). https://doi.org/10.1007/s11665–020-05093–1.
[63] H. Sun, Y. Sun, R. Zhang, M. Wang, R. Tang, Z. Zhou, Hot deformation behavior and microstructural evolution of a modified 310 austenitic steel, Mater. Des. 64 (2014) 374–380, https://doi.org/10.1016/J.MATDES.2014.08.001
[64] A. Dehghan-Manshadi, M.R. Barnett, P.D. Hodgson, Hot Deformation and Recrystallization of Austenitic Stainless Steel: Part I. Dynamic Recrystallization, (n.d.). https://doi.org/10.1007/s11661–008-9512–7.
[65] X.Y. Chi, X.M. Chen, Y.C. Lin, X.Z. Lu, Evolution of annealing twins in a hot deformed nickel-based superalloy, Mater. (Basel) 15 (2022) 1–13, https://doi.org/10.3390/ma15010007
[66] R. Daniel, J. Zalesak, I. Matko, W. Baumegger, A. Hohenwarter, E.P. George, J. Keckes, Microstructure-dependent phase stability and precipitation kinetics in equiatomic CrMnFeCoNi high-entropy alloy: role of grain boundaries, Acta Mater. 223 (2022), https://doi.org/10.1016/J.ACTAMAT.2021.117470
[67] L. Li, R.D. Kamachali, Z. Li, Z. Zhang, Grain boundary energy effect on grain boundary segregation in an equiatomic high-entropy alloy, Phys. Rev. Mater. 4 (2020) 53603, https://doi.org/10.1103/PhysRevMaterials.4.053603